



Delft University of Technology

## Pre-cracking development of weld-induced squats due to plastic deformation

### Five-year field monitoring and numerical analysis

Deng, Xiangyun; Li, Zili; Qian, Zhiwei; Zhai, Wanming; Xiao, Qian; Dollevoet, Rolf

**DOI**

[10.1016/j.ijfatigue.2019.06.013](https://doi.org/10.1016/j.ijfatigue.2019.06.013)

**Publication date**

2019

**Document Version**

Final published version

**Published in**

International Journal of Fatigue

**Citation (APA)**

Deng, X., Li, Z., Qian, Z., Zhai, W., Xiao, Q., & Dollevoet, R. (2019). Pre-cracking development of weld-induced squats due to plastic deformation: Five-year field monitoring and numerical analysis. *International Journal of Fatigue*, 127, 431-444. <https://doi.org/10.1016/j.ijfatigue.2019.06.013>

**Important note**

To cite this publication, please use the final published version (if applicable).  
Please check the document version above.

**Copyright**

Other than for strictly personal use, it is not permitted to download, forward or distribute the text or part of it, without the consent of the author(s) and/or copyright holder(s), unless the work is under an open content license such as Creative Commons.

**Takedown policy**

Please contact us and provide details if you believe this document breaches copyrights.  
We will remove access to the work immediately and investigate your claim.

***Green Open Access added to TU Delft Institutional Repository***

***'You share, we take care!' – Taverne project***

***<https://www.openaccess.nl/en/you-share-we-take-care>***

Otherwise as indicated in the copyright section: the publisher is the copyright holder of this work and the author uses the Dutch legislation to make this work public.



## Pre-cracking development of weld-induced squats due to plastic deformation: Five-year field monitoring and numerical analysis

Xiangyun Deng<sup>a</sup>, Zili Li<sup>a,\*</sup>, Zhiwei Qian<sup>a</sup>, Wanming Zhai<sup>b</sup>, Qian Xiao<sup>c</sup>, Rolf Dollevoet<sup>a</sup>



<sup>a</sup> Section of Railway Engineering, Faculty of Civil Engineering and Geosciences, Delft University of Technology, Stevinweg 1, 2628 CN Delft, the Netherlands

<sup>b</sup> State Key Laboratory of Traction Power, Train and Track Research Institute, Southwest Jiaotong University, Chengdu 610031, China

<sup>c</sup> Key Laboratory of Ministry of Education for Conveyance and Equipment, East China Jiaotong University, Nanchang 330013, China

### ARTICLE INFO

**Keywords:**  
Welds-induced rail squats  
Field observation  
Finite element simulation  
Varying hardness distribution  
Differential plastic deformation  
Dynamic contact force

### ABSTRACT

Weld-induced squats are a major damage type in high-speed railways as well as in conventional railways. They incur high maintenance costs and endanger operational safety. This paper first presents and analyzes five-year continual field monitoring observations and measurements of squats at rail welds. A hypothesis of the formation and development process of the squats is proposed, which includes three steps. Steps 1 and 2 are pre-cracking, and Step 3 is post-cracking. To verify the pre-cracking process, a three-dimensional (3D) finite element (FE) model is then built up to simulate the vehicle-track interaction with detailed consideration of the local wheel-rail frictional rolling contact. Not only dynamic contact forces but also plastic deformation and wear are calculated. Starting from a smooth rail surface with varying yield stress derived from field-measured hardness, the numerical analysis confirms the hypothesis that the varying hardness at heat-affected zones (HAZs) leads to initial V-shaped irregularities due to differential plastic deformation. Afterward, the surface irregularities excite the dynamic longitudinal contact force, which in turn produces a W-shaped surface pattern through further differential plastic deformation. The growth of the W-shaped pattern leads to the formation of squats. This work provides insight into the squat formation process at rail welds and suggests that welding quality control in terms of hardness variation in the HAZs could reduce or even avoid squats. Early detection of squats with dynamics-based methods is possible.

### 1. Introduction

Welding has been widely employed to join rails in railway tracks. However, the welding process can introduce changes in the rail microstructures and its mechanical properties, as well as geometric irregularities. Particularly, during the welding process, heat-affected zones (HAZs) are produced in the vicinity of the weld metal (WM) [1]. The heat inevitably alters the microstructures in the HAZs, leading to phase transformation, mostly causing a lower hardness distribution within the HAZs [2]. As a result, a spatially inhomogeneous material properties distribution is introduced along the rail [3]. Moreover, geometric irregularities often excite high dynamic wheel-rail contact forces. These factors contribute to localized rolling contact fatigue (RCF) damage both at and under the rail surface. Several types of RCF damage have been identified at welds, including squats in the rail surface and the damage in the rail web.

Many efforts have been made to limit and reduce RCF at welds. Ilić et al. [4] proposed that heat treatment could improve the mechanical

properties of welds. The influences of residual stress and porosity on crack initiation at rail web were studied by Skyttebol et al. [5] and Fry et al. [6]. Moreover, some studies, such as the investigation performed by Desimone and Beretta [7], focused on crack propagation in the rail web at welds. A further concern is the vehicle-track dynamic interaction at the railhead in the vicinity of welds because the dynamic forces resulting from the initial irregularities of welding would significantly influence RCF damage. Steenbergen and Esved [3] studied the interaction at welds using numerical simulations with consideration of the measured geometry of welds. Wen et al. [8,9] studied the vehicle-track interaction and the plastic deformation at both a straight track and a curved track. They found that the initial irregularities of welds had a significant influence on the dynamic contact forces. An additional concern is the wheel-rail dynamic interaction with considering actual measured rail surface geometry in welds under operation condition. For instance, Gao et al. [10] analyzed measured rail surface geometry of welds in a Chinese high-speed railway and proposed a model to study the dynamic interaction at the welds. They found that the weld

\* Corresponding author.

E-mail address: [Z.Li@tudelft.nl](mailto:Z.Li@tudelft.nl) (Z. Li).

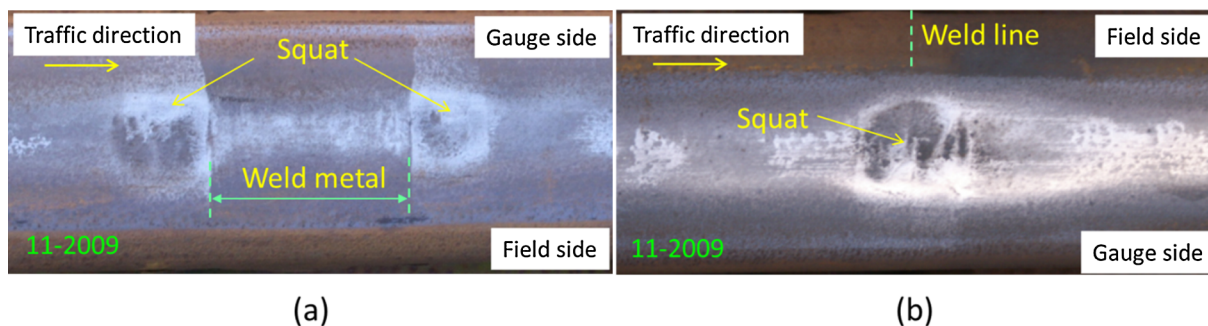


Fig. 1. Typical squats at welds: (a) duo squats at a thermite weld; (b) a single squat at a flash butt weld.

irregularities dominantly appeared in short-wavelength form, which have considerable impacts on wheel-rail dynamic responses. Recently, Sh. Sichani and Bezin [11] presented a model to estimate the evolution of geometry at welds.

Despite these works on rail welds, few studies are found on rail squats at welds. Squats are a main type of rail RCF defect [12,13]. They are identified as local depressions in the rail surface with cracks [14]. Squats are mostly observed on tangent tracks and shallow curved tracks. A series of investigations by Li et al. [15–20] reported that squats initiate from various sources, such as welds, indentations, short pitch corrugation, insulation joints and crossings. As one of the main initiation sources, welds have been shown to contribute to the formation of a large population of squats [15]. For instance, it was found through field surveys in the Netherlands that 10–15% of squats were caused by welds [17]. They were observed at both thermite welds and flash butt welds, as shown in Fig. 1. At a thermite weld, duo squats are frequently observed, and at a flash butt weld, there is usually only a single squat. The accompanying cracks at squats can propagate in the rail and may ultimately lead to rail break. On a European railway network, approximately 15,000 welding repairs have to be performed every year because of squat damage [20]. Grinding is a technique widely used to remove squats, protecting the rail from further degradation. However, grinding is expensive and influences the availability of tracks. A good understanding of squat formation and development helps in developing and deploying efficient control measures against squats in the early stage, reducing maintenance costs and improving availability.

Through field observations and numerical analysis, Li et al. [15,16] suggested that the initiation and development of squats are related to high-frequency vehicle-track dynamic interaction forces. The frequency is determined by certain eigen characteristics of the vehicle-track system and the length of rail surface irregularities. They explained how a small surface irregularity under dynamic forces develops into a typical squat with the characteristic of a two-lung-like shape. Li et al. [16] also proposed that squats at welds are caused by differential plastic deformation and wear and the resulting surface irregularity because of HAZs. However, the specific formation and development process observed from continual field monitoring has not been provided, and the causes taking into account differential plastic deformation and wear have not been studied either.

Field observation is an effective approach to study rail surface damage. Recently, Deng et al. [21] presented an extensive five-year continual field monitoring study on corrugation-induced squats. The development process of squats from early small surface depressions to the typical two-lung shape, as well as the growth process of the associated geometry and cracks, was presented, alongside a discussion of the causes of the impact force of wheels on rails that is responsible for the development of the geometry. These processes and causes can explain the formation of corrugation-induced squats. However, squats induced by welds have initiation sources other than corrugation, and their formation needs further investigation.

The present work investigates the mechanism of squat initiation and growth at rail welds through both field observations and numerical pre-cracking simulations. To this end, continual field monitoring observations and measurements were first performed to identify the development features of the squats. Based on the observations and considering the effects of the dynamic wheel-rail forces on squat development presented in [15], a hypothesis for the development process of the squats is proposed. Afterward, a three-dimensional (3D) finite element (FE) dynamic vehicle-track interaction model with detailed consideration of wheel-rail contact is employed to verify the hypothesis by computing the dynamic contact forces, stresses, plastic deformations and wear. The FE model considers field-measured rail hardness and surface irregularities.

## 2. Field monitoring observations and measurements

To investigate squat initiation and development, a five-year field monitoring was performed in the period from 2007 to 2012 on a straight track located at Steenwijk in the Netherlands. One-directional traffic ran on the selected track. A detailed description of the monitoring is presented in [21]. Briefly, ten rounds of observations were made at intervals of approximately six months during the monitoring. Squats caused by various sources, such as corrugation, welds and wheel burns, were monitored. During each observation round, selected squats were photographed, and their cross-sectional profile and vertical-longitudinal profiles were measured using MiniProf and RailProf devices, respectively. Among them, RailProf measures at every 5 mm along the rail with a maximum error of  $\pm 0.03$  mm for profile deviation up to 0.5 mm and a maximum error of  $\pm 5\%$  of the measured value for profile deviation between 0.5 mm and 1.5 mm. In the present work, squats caused by welds on the monitored track are the focus. Some other welds from a number of one-off field observations and measurements at Nijeveen and Zaandam in the Netherlands are further employed to illustrate the development of squats at welds. Both thermite welds and flash butt welds are discussed.

Below, it is shown in Section 2.1 that the weld-induced squats occurred at the HAZs. Section 2.2 shows that geometrical irregularities had already developed at the HAZs before the squats occurred. Section 2.3 shows that the squats and the irregularities have a strong correlation with the hardness variation in the HAZ. These observations form the basis for the hypothesis made in Section 3.

### 2.1. Squats with cracks at welds

#### 2.1.1. Squats at thermite welds

Fig. 2 shows duo squats at a thermite weld in the first, fifth and sixth observations of the monitoring at Steenwijk. The rail was ground between the fifth and the sixth observations [21]. The photos are aligned with the two fusion lines (the red dashed lines) that border the WM and the parent rail material. The distance between the two lines outside the running band should be constant during the service life of the weld

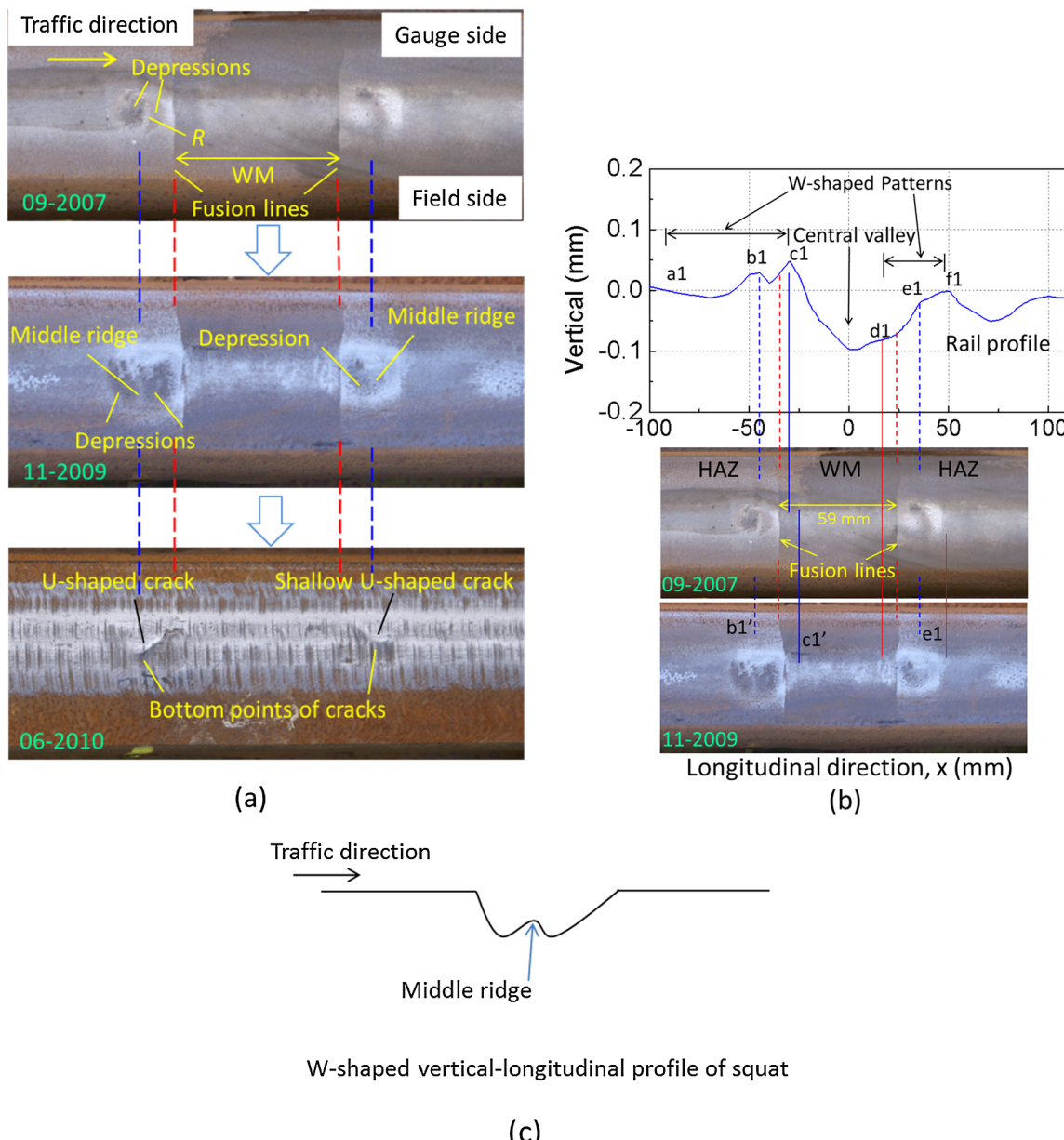


**Fig. 2.** Observations and measurements of a thermite weld with duo squats. Red dashed lines indicate fusion lines and blue dashed lines indicate the locations of middle ridges. (a) The squat in the first (09-2007), fifth (11-2009) and sixth (06-2010, after a rail grinding) observations; (b) Measured rail profile (the blue solid line) in the 09-2007 observation (Red solid lines align d1 and f1 with features in the photos to determine the dimension of the right squat); (c) Illustrative W-shaped vertical-longitudinal profile across a typical squat. (For interpretation of the references to colour in this figure legend, the reader is referred to the web version of this article.)

(approximately 59 mm in the current case) so that it can be used as a reference for aligning the photos.

In 11-2009, the squat on the left side already had the typical two-lung shape of squats with a slightly shining middle ridge, b1', between the two lungs, which were dark depressions. Because the depressions were lower than the normal rail surface and the ridge was higher than the depressions, the vertical-longitudinal profile across the squat would have a W-shaped pattern, as illustrated in Fig. 2(c). The vertical-longitudinal profile measured in 09-2007 (Fig. 2(b)) shows that a W-shaped pattern a1b1c1 already existed as early as at the first observation. A W-shaped pattern consists of two V-shaped dips, with one between the WM and the ridge (b1c1) and the other (a1b1) on the other (far) side of the ridge.

The defect on the right side did not yet bear the typical appearance of mature squats in 11-2009, and a middle ridge could be seen only by

experienced eyes in the photo. The 06-2010 photo, however, reveals a primary crack typical of squats [21]. The primary cracks of squats usually develop into a U-shape when squats are in their severe stage, e.g., see Li et al. [16] and Deng et al. [21], though in the 06-2010 photo the primary cracks of both defects did not yet have a full U-shape, but only an early and, thus, shallow and incomplete U-shape. The middle ridge of a squat usually starts from the bottom point of the U and extends to the opposite side of the squat [21], and this is the case for both defects in Fig. 2. Thus, the right defect was also a squat.

In the measured profile of Fig. 2(b), a clear W-shaped pattern was missing at the right squat. A peak, e1, however, existed at the location of the middle ridge. Looking at the photos, an indication of a dark depression can clearly be seen in the 11-2009 photo between d1 and e1. In view of this depression and the crack that had a size comparable to that of the left squat, it is reasonable to conclude that a V-shaped dip

should exist between d1 and e1 in 09-2007. Indeed, a shallow V-shape can be distinguished between d1 and e1 in the big central valley. A V-shaped dip should also be in formation between e1 and f1, as indicated by the less bright area between them in the 11-2009 photo. Thus, there was a W-shaped pattern at the right squat, too.

Further, a bright strip marked by R is visible in the left squat in the 09-2007 photo. It looks like a middle ridge but was not precisely at the location of the middle ridge b1' (see the 11-2009 photos). This bright strip would probably be caused by a varying hardness distribution, and it became erased or shifted to the location of the middle ridge during the growth of the squats, determined by the wavelength of the dynamic contact force, as will be discussed in [Section 6.1](#).

At the time of 09-2007, cracks visible to the naked eye already existed in the surface of both squats. The cracks were in the V-dips between the ridges and fusion lines and had not developed into the V-dips on the far sides in 06-2010. It is therefore reasonable to conclude that these two V-dips on the far sides were not caused and influenced by the cracks that had developed by 09-2007. In [Section 2.2](#), it will be shown that such V-shaped dips already exist before any visible surface cracks exist.

[Fig. 3](#) shows another instance of duo squats at a thermite weld from the same monitoring site at Steenwijk. The length of the WM is approximately 60 mm. Note, although this weld is located on the same track as the one in [Fig. 2](#), the length of WM is different because of the inherent limitations of the welding process used and operator dependency [22]. At this weld, the W-shaped pattern was more evident than that in [Fig. 2](#) at the time of the first observation. They continued to grow and became two typical squats by the time of the fifth observation. Cracks also grew with the development of the geometry.

It is not necessary to always have two squats simultaneously at a thermite weld. Single squats were also observed, such as the example in

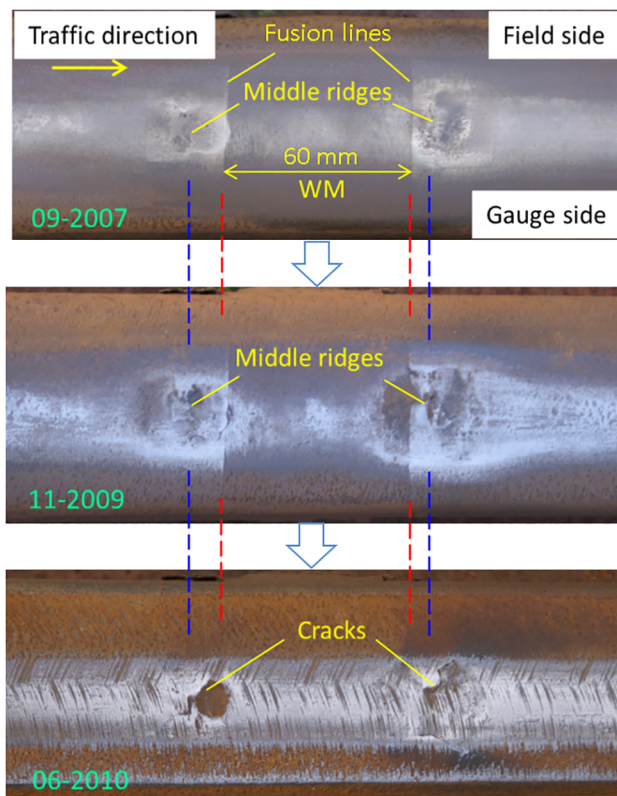


**Fig. 3.** Another example of thermite welds with duo squats in the first (09-2007), fifth (11-2009) and sixth (06-2010, after a rail grinding) observations, where the WM was approximately 60 mm in length. This is the same squat as that shown in [Fig. 1\(a\)](#).



**Fig. 4.** One single squat at a thermite weld with shorter WM (from [15]).

[Fig. 4](#). At this thermite weld, the length of the WM looks to be much shorter than those in [Figs. 2](#) and [3](#), so that only a single squat could occur. The length of WM and the characteristic length of the hardness variation at welds often determine whether one or two squats occur at a weld. This issue will be further discussed in [Sections 2.3 and 6](#).

Another explanation for having only one squat at a thermite weld is that the welding quality is good in the non-squatting HAZ of the weld, where there is no hardness variation or the magnitude of the variation is very small. The length of the WM in [Fig. 5](#), for instance, was approximately 65 mm, which is not smaller than that in [Figs. 2 and 3](#). However, only a single squat occurred, and there was no sign of squatting in the right HAZ. This observation thus inferred that the welding quality in the right HAZ was good, so that the resulting differential deformation and wear needed to fulfill the hypothesis in [Section 3](#) was not large enough to induce a squat.

Indeed, many thermite welds do not cause squats. Thus, if the welding quality is well controlled, e.g., in terms of hardness variation, it is possible to greatly reduce squats at thermite welds.

### 2.1.2. Squats at flash butt welds

[Fig. 6\(a\)](#) shows a flash butt weld with a single squat. In a flash butt weld, the HAZs are nominally symmetrical about the weld line (WL) because of the absence of WM [23]. The squat should have developed from a W-shaped hardness variation distribution, see [Fig. 6\(b\)](#) for a typical W-shaped hardness distribution of virgin flash butt welds, where each of the V-dips of the W corresponds to one of the HAZs. At the time of the first observation (09-2007), the W-shaped pattern of the squat was identifiable by the shining middle ridge that was along the weld line. The W-shaped pattern then grew to a two-lung-shaped squat with a much clearer middle ridge by the time of the fifth observation (11-2009).

A network of cracks can be seen after grinding in the 06-2010 photo, with a U-shaped crack (dashed line in the inset of [Fig. 6\(a\)](#)) on the gauge side, two transverse cracks (solid lines) along the ridge and a longitudinal crack (dotted line) on the field side. In this case, it is not

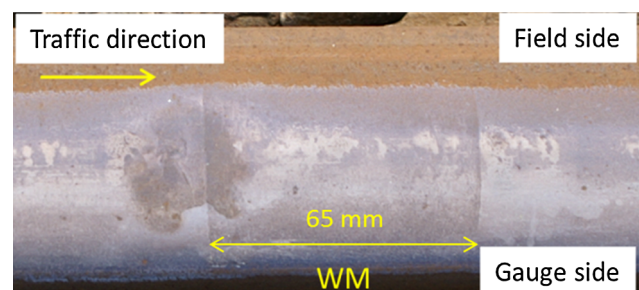
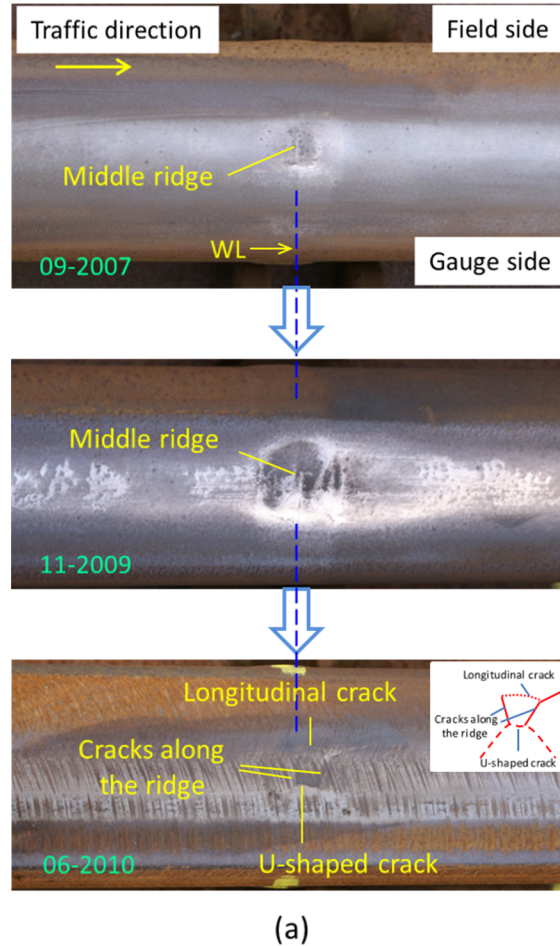
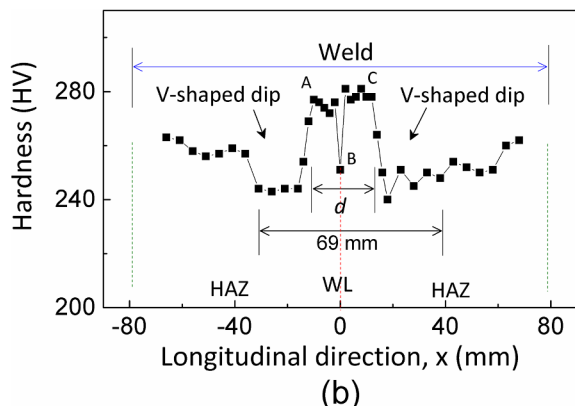


**Fig. 5.** Single squat at a thermite weld observed at Nijeveen in the Netherlands.



(a)



(b)

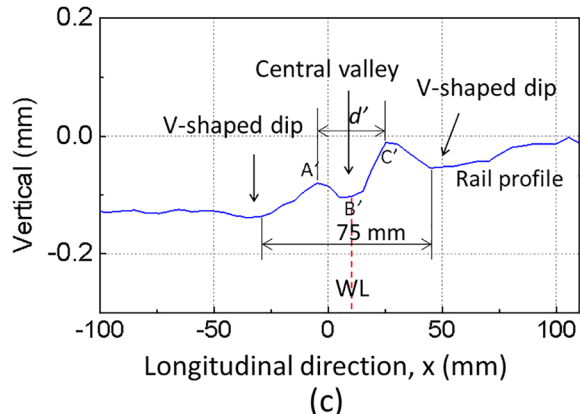


**Fig. 6.** (a) The growth process of a squat at a flash butt weld (with only one single squat). This is the same squat as that shown in Fig. 1(b). WL stands for Weld Line; (b) W-shaped hardness distribution measured at a virgin flash butt weld. The two V-shapes are on the two sides of the weld line; (c) Measured vertical-longitudinal rail profile in 09-2007. The length  $d'$  of  $A'B'C'$  corresponds to the width  $d$  in the hardness plateau ABC of (b), but they are not necessarily the same.

clear whether it was the U-shaped crack or those along the ridge that were the primary cracks, as locations of both the U-shaped crack and of the ridge were shining in the 09-2007 photo, indicating large impacting stress [21]. The two cracks along the middle ridge were relatively apart from each other, most probably due to the width  $d$  of the hardness plateau (ABC) in the middle of the weld (Fig. 6(b)). The width  $d$  is determined by the characteristic length of the hardness variation  $L_d$  that will be discussed in Section 2.3 with Fig. 9. Large sudden hardness change can be a source of cracking.

Rail surface evolves due to differential plastic deformation and wear; the corresponding locations of ABC might change and they

became  $A'B'C'$  in the vertical-longitudinal rail profile in Fig. 6(c) measured at the weld in 09-2007. Its length  $d'$  is determined by the wavelength of the dynamic force, which is about 30 mm and is determined by the eigen characteristics of the local vehicle-track system, see [15,24] and Section 3 of this paper. The pattern of the measured profile followed the typical hardness distribution of Fig. 6(b), with a narrow central valley at  $B'$  corresponding to the hardness drop B at the WL in the middle of the hardness plateau ABC. As the distance of approximately 30 mm between  $A'$  and  $C'$  is much narrower than those of the thermite welds ( $> 45$  mm), there was only a single squat in this location.

So far in our observations, only single squats have been found at flash butt welds. This is unlike the cases for thermite welds where two squats were usually observed.

### 2.1.3. Summary

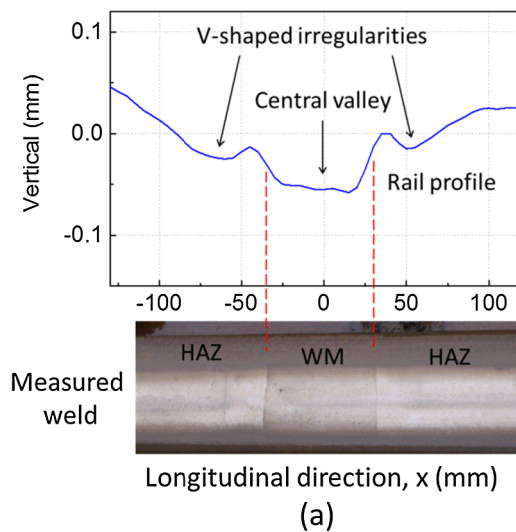
These field monitoring observations show that squats initiated at both thermite welds and flash butt welds. They should have developed from W-shaped pattern in the HAZs, and then grown into the typical two-lung shape with apparent cracks. Duo squats usually occurred at thermite welds, though cases of a single squat were also observed, probably depending on the length of the WM and the quality of the weld. Single squats were usually observed at flash butt welds, probably because the length between the two hardness dips of the two HAZs was too small to allow two squats to develop separately on the two sides of the WL.

## 2.2. Welds without cracking

In the aforementioned continual field monitoring, squats in the stages before crack initiation were not observed at welds. The profiles shown in Figs. 2(b) and 6(c) were measured when visible cracks were already present. To see the development of squats before crack initiation, one-off field observations and measurements of several thermite welds were performed on the track at Zaandam in the Netherlands at the end of 2011. The surface irregularities of the examined welds are considered representative of pre-cracking squats, as they had in common the V-shaped dips in HAZs, which are presumably the initiation source of squats, as discussed in Section 2.1.

Fig. 7 shows two of the thermite welds and their measured profiles, respectively. The profiles are aligned with the welds. Two V-shaped dips (irregularities) in the HAZs and one central valley at the WM were observed. It is worth mentioning that the maximum depth of the irregularities might be larger than the measured depth because the profile was measured at the rail center, whereas the irregularities usually have an offset from the rail center because the running band is usually not precisely in the middle of rails. At the time of the observation, no cracks were found in the surface at the two welds, which indicates that surface irregularities at welds indeed exist before crack initiation.

Fig. 8 shows another thermite weld and its measured profile. No cracks were found in the rail surface. The profile was generally similar to those in Figs. 2 and 7, with a central valley and a V-shaped dip on each side. In Figs. 7(b) and 8, three of the V-shaped dips were



(a)

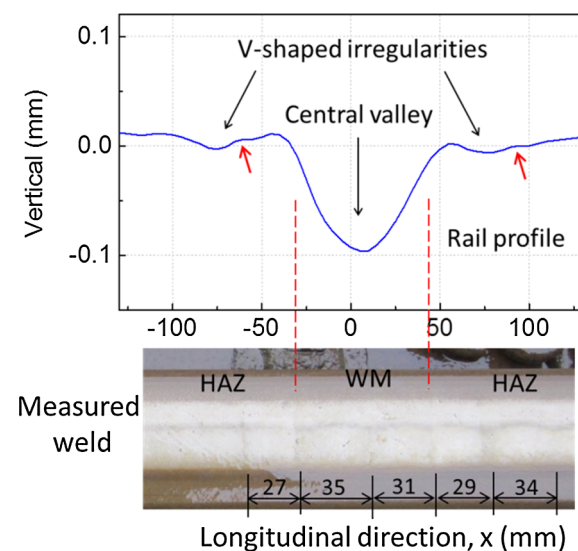
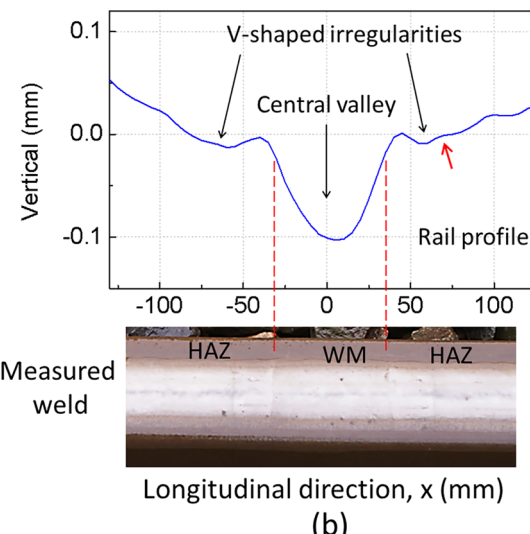


Fig. 8. Measured profile of a thermite weld without cracks: V-shaped irregularities were in both HAZs (the length of WM was approximately 73 mm). If the two small peaks indicated by the two red arrows are considered, each of the V-dips was evolving towards a W-shape. Waves were visible on the rail surface with the wavelength indicated in the photo. (For interpretation of the references to colour in this figure legend, the reader is referred to the web version of this article.)

developing towards W-shaped patterns.

Comparing the photos and measured profiles in Figs. 2, 7 and 8, it is observed that the severity of the surface irregularities is in the following decreasing order. (1) Fig. 2 is the most severe, with squats and cracks. Its left squat is more severe than the right, as judged from both the photos and the profile – the left squat already had a clear W-shaped profile and the W-shape of the right squat was not yet so clear. (2) Fig. 8 had clear and continuous waves on the rail surface, with indications in the profile that W-shaped patterns were in formation in both HAZs. (3) Fig. 7 did not have a clearly continuous wave pattern on the rail surfaces, with only one of the four HAZs showing an indication that W-shaped patterns were in formation. These consistent observations further support the inference that weld-induced squats initiate from V-dips without cracks, which further evolve into the W-shape and then the



(b)

Fig. 7. Two thermite welds without cracks and their profiles. The length of the WM is approximately 64 mm in (a) and 67 mm in (b). If the small peak indicated by the red arrow is considered, the V-dip on the right side in (b) was evolving towards a W-shape. (For interpretation of the references to colour in this figure legend, the reader is referred to the web version of this article.)

typical two-lung shape with cracks.

In the profile measurements of Figs. 2, 7 and 8, large central valleys existed at the WM. In practice, this is not necessarily always the case. Depending on the welding process and finish grinding, random surface geometry deviations are created. Bumps, instead of valleys, could occur at the WM, such as that shown in Fig. 4 of [10]. In view of the fact that mature squats all have the characteristic two-lung shape, irrespective of such randomness, it is inferred that squats should have not been caused by the large central valleys or bumps at the WM and that surface deviations are not essential for the formation of squats. Instead, it should be the HAZ hardness distribution and the associated wavelength that are decisive. This issue will be examined with the help of numerical simulation in Sections 4, 5 and 6.

### 2.3. Hardness distribution at welds

Li et al. [15] proposed that the initiation of squats at welds is related to the initial hardness distribution. They also provided the general longitudinal distributions of the hardness in the HAZs for both thermite welds and flash butt welds, as schematically illustrated in Fig. 9(a). The hardness at welds varies because the welding material is different from the parent material and the welding process produces a lot of heat. The heat changes the hardness of the parent rail materials in the HAZs, mostly causing a lower hardness distribution within the HAZs. As a result, a spatially varying hardness distribution with two dips is introduced along the rail. This distribution may be characterized by the length  $L_d$  in Fig. 9(a), the distance between the two dips. This characteristic length is for thermite welds affected by the WM and HAZs, and it can be larger than 65 mm. This is because that the distance (length  $L$  in Fig. 9(a)) between the fusion line and the dip of the

hardness is approximately 20 mm [25] on each side, and the WM can be longer than 25 mm, since the standard weld gap is 25 mm and wider gaps may occur [2]. The characteristic length of flash butt welds is  $L_d = 2L$  (Fig. 9(a)) and it is nominally 20–45 mm based on [23]. The measured hardness distributions for a virgin thermite weld and a virgin flash butt weld shown in Fig. 9(b) and (c) confirm these schematic distributions and nominal lengths of initial hardness variation.

The hardness dips in the HAZs correspond to the surface irregularities in the HAZs in Figs. 7 and 8 and at the squats in Fig. 2. This result shows that the formation of the initial surface irregularities and squats can be related to the hardness distribution. This issue will be analyzed in Sections 4 and 5.

Considering the discussions of Sections 2.1, 2.2 and 2.3, the correlation between the hardness distribution and squat formation suggests that the frequent duo squats at thermite welds and single squats at flash butt welds should be mainly affected by the characteristic length  $L_d$  of the hardness variation, which is influenced by the lengths of the WM and HAZs. This issue will be further discussed in Section 6.

### 2.4. Summary of the observations and measurements

Squats were observed at both thermite welds and flash butt welds. They initiated from V- and W-shaped surface irregularities, which were related to the initial varying hardness of HAZs. Other initial surface geometry deviations due to characteristics such as imperfect welding and finish grinding should not be essential for the formation of irregularities and, therefore, squats. Duo squats usually occurred at thermite welds due to a longer characteristic length of hardness variation, though single squats were also observed at times. Single squats were observed at flash butt welds due to the absence of WM and, thus, a

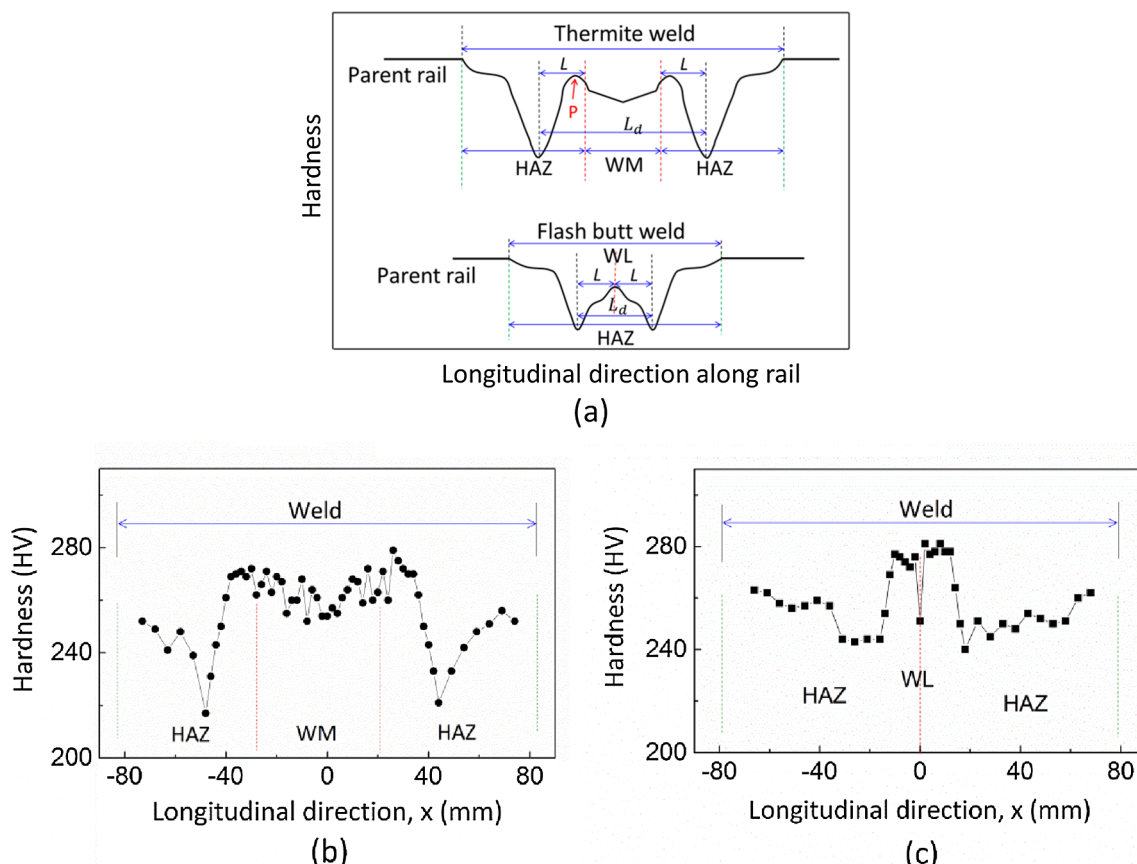


**Fig. 9.** Distributions of the hardness: (a) at a thermite weld and a flash butt weld, respectively (schematic diagram; the red dashed lines indicate the fusion lines); (b) at a virgin thermite weld (measured); (c) at a virgin flash butt weld (measured; this hardness distribution is the same as that in Fig. 6(b)). (For interpretation of the references to colour in this figure legend, the reader is referred to the web version of this article.)

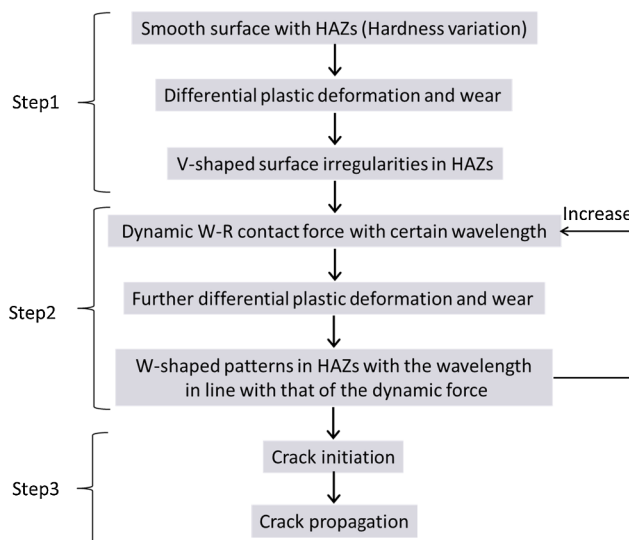


**Fig. 10.** Development process of squats at welds.

shorter length of hardness variation. Thus, the number of squats (duo or single) caused by a weld is determined by the characteristic length of the hardness variation, which is related to the length of the WM and of the HAZs.

### 3. Hypothesis of squat formation at welds

Based on the field observations and measurements discussed above and considering the effect of the dynamic wheel-rail contact forces on squats development presented in [15], a formation process of squats at welds is hypothesized as shown in Fig. 10. It can be roughly divided into three steps according to the dominant driving mechanisms.

In the first step, surface irregularities initiate in the HAZs from the smooth rail surface through the accumulation of differential deformation and wear due to the varying material properties under cyclic loadings. The surface irregularities have a shape similar to that of the initial hardness distribution along the rail. Usually, a roughly V-shaped irregularity appears in each HAZ.

In the second step, a V-shaped irregularity excites a high dynamic contact force with a wavelength determined by the eigen characteristics of the local vehicle-track system and the length of the irregularity [15]. The dynamic force in turn produces further differential plastic deformation and wear so that the V-shaped irregularity develops into a W-shaped pattern, the wavelength of which is determined by that of the dynamic force [15]. The continuous development of the W-shaped patterns increase the dynamic force and the resulting stresses and

strains at the same location, leading to a loop of positive feedback, with increasing W-shaped damage and progressive rail fatigue.

In the third step, crack initiation eventually occurs at the location where the values of the damage parameters are the highest, and then cracks propagate in the surface and into the rail.

The distance between the two dips in the hardness distribution is 20–45 mm for flash butt welds, according to Section 2.3. This characteristic length is in close agreement with the typical wavelength of 20–40 mm of squats determined by the Eigen characteristics of the local vehicle-track system [15]. The dynamic contact force excited by the differential plastic deformation and wear at one of the two dips can be in-phase with the differential plastic deformation and wear at the other dip. The two V-shapes at the two dips can combine with each other to form a W-shaped pattern that eventually becomes a single typical squat.

On the other hand, the characteristic length of the initial hardness variation at thermite welds is often greater than 65 mm. This length is much greater than the 20–40 mm wavelength of squats. As a result, the two V-shapes at the two dips cannot combine with each other to form a W-shaped defect. Instead, each V-shaped dip will develop into a W-shaped pattern, so that two W-shaped patterns are generated.

Thus, according to the hypothesis, the number of squats caused by a weld will be determined by the characteristic length of the spatially varying hardness distribution. If the characteristic length is much larger than the wavelength of typical squats, two squats may occur at a weld. This is frequently the case with thermite welds. Otherwise, only one squat occurs, for instance, at flash butt welds.

In the present work, the numerical simulations in Sections 4 and 5 will verify this hypothesis of squat development before crack initiation, i.e., Step 1 and Step 2. The crack initiation and propagation will be studied in another investigation.

### 4. Numerical model

In this section, a 3D FE dynamic vehicle-track interaction model is applied to verify the hypothesis of the development of squats at welds due to differential plastic deformation and wear before crack initiation. The thermite weld is the focus.

#### 4.1. FE model

A 3D FE dynamic vehicle-track interaction model is created using the ANSYS/LS-DYNA software to calculate the contact forces, the stresses and the deformation at a rail weld. A schematic view of the model is shown in Fig. 11(a). In this model, half of a typical wheelset and a straight track are considered. The primary vehicle suspension is modeled as a group of springs and dampers, and the vertical load from the carriage is imposed through a mass block. Between the rail and the sleepers, groups of springs and dampers are inserted to represent rail

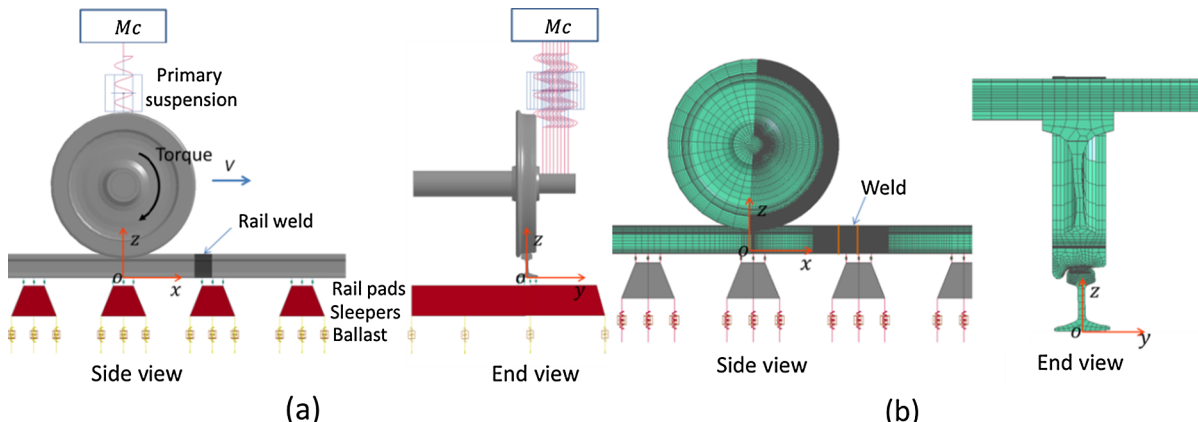


**Fig. 11.** FE vehicle-track interaction model: (a) FE model of wheel-rail rolling contact at a rail weld; (b) mesh of the model.

pads. Below the sleepers, the ballast is modeled as a group of springs and dampers. The stiffness and damping coefficients of these springs and dampers are taken from [26]. The static wheel load is 116.48 kN according to [26] including the 540 kg weight of the wheel. The standard wheel profile S1002 and a worn rail profile measured near the squat of Fig. 2 are employed. The nominal rail inclination of 1/40 is applied. The dynamic response arising from the vehicle-track interaction is considered. The accuracy of the approach is validated by Mollova et al. [27] when studying the detection of squats.

Contact between the wheel and the rail is determined by a surface-to-surface contact-searching scheme [28]. It is based on a master-slave algorithm. The kinematic contact condition is enforced by a penalty method [29]. The Coulomb friction law is employed. The accuracy of this calculation method for contact problems has been validated by Zhao et al. [30,31] and Deng et al. [32].

The 3D 8-node solid brick element is applied to discretize the wheel, the rail and the sleepers. To improve the accuracy of the stress calculation while maintaining a reasonable computational time, a non-uniform mesh is employed to both the rail and the wheel, see Fig. 11(b). The mesh fineness at the weld and at the part of the wheel that is in contact with the weld is approximately 1 mm per element. The Lagrangian dynamic non-linear analysis is conducted using an explicit integration approach, as it is intrinsically suitable for simulating dynamic rolling contact processes [30].

A torque is applied to the axle of the wheel to produce traction to drive the wheel rolling. The traveling speed of the wheel is 140 km/h. The frictional coefficient  $f$  is 0.6, and the traction coefficient is 0.35 [19]. In this study, one wheel passage is simulated, and the resulting stresses and deformation in the rail at the weld are calculated and analyzed.

#### 4.2. Material properties at the weld

In this work, a thermite weld with the measured hardness distribution shown in Fig. 9(b) is analyzed. The hardness variation is distributed over a length of approximately 160 mm, with the distance between the two hardness dips of the HAZs being 92 mm. It thus should be sufficiently long to produce two squats at the two HAZs, according to the preceding discussion. The hardness distribution is measured to determine the yield stress by the formula below [33],

$$\sigma_y = \frac{H_V}{3}(0.1)^n \quad (1)$$

where  $H_V$  is the Vickers hardness,  $\sigma_y$  is the yield stress, and  $n$  is the strain hardening coefficient. The value of  $n$  for Grade 900A rail steel is 0.225, which is determined by the initial yield stress of 546 MPa and the corresponding hardness of 275 [34,35]. The hardness is converted to the yield stress by Eq. (1). The converted yield stress is linearly interpolated at approximately 0.5 mm, then smoothed using the Adjacent-Averaging method with a window of 10 points. The resulting distribution of the yield stress is shown in Fig. 12(a) and serves as an input to the FE model (Fig. 12(b)). The middle of the distribution is at the rail position of 580 mm. This yield stress distribution is applied throughout the whole rail height. The hardness of the surface layers of both the parent rail and the wheel is set to 280  $H_V$  based on field measurements, and therefore the corresponding yield stress is 556 MPa. The initial yield stress of 546 MPa is applied to the subsurface of the wheel and rail.

The non-linear isotropic/kinematic hardening model originally proposed by Lemaitre and Chaboche [36] is applied to both the wheel and the rail. In this model, five parameters are defined to characterize the material behavior: the Young's modulus  $E$ , the yield stress  $\sigma_y$ , the isotropic plastic hardening modulus  $H$ , the kinematic hardening modulus  $C$  and the kinematic hardening parameter  $\gamma$ . The yield stress is determined as shown above, and the other parameters are obtained according to [37,38]. They are given in Table 1 and are applied to both

the wheel and the rail for Steps 1 and 2, as will be discussed in Section 4.4.

#### 4.3. Surface deformation and wear

Plastic deformation and wear are the two direct causes of rail surface deformation [39], and thus the causes of the evolution of rail surface irregularities. The surface nodal permanent displacement is the plastic deformation. It is computed directly by the FE simulation of a wheel passage, and the wear is calculated based on the surface shear stress and micro-slip using the Archard wear model [40,41] as follows.

The surface shear stress  $\tau_i$  and micro-slip  $v_i$  at each time step  $i$  are obtained from the FE simulation. According to the Archard wear model, a material removal of depth  $d$  due to wear is calculated for each node in the running band by:

$$d = \frac{K}{H_V f} \int_0^{t_0} \tau(t) ds = \frac{K}{H_V f} \int_0^{t_0} \tau(t)v(t)dt = \frac{K}{H_V f} \sum_0^M \tau_i v_i \Delta t \quad (2)$$

where  $t_0$  is the duration that a node passes a contact patch.  $\tau(t)$  is the shear stress at a node on the rail surface at time  $t$  and is updated after each time step in the solution procedure.  $ds$  is the increment of the sliding distance of the rail node relative to the wheel contact surface, and is calculated by multiplying the micro-slip  $v(t)$  by the time increment  $dt$ .  $\Delta t$  is the discretized form of  $dt$ .  $M$  is the total number of time steps.  $H_V$  is the material hardness defined in Section 4.2. The wear coefficient  $K$  is a constant, the value of which is taken as 3.56e-4 according to [42].

#### 4.4. Simulation steps

It takes thousands of wheel passages to form a squat through cyclic plastic deformation and wear. Simulating all these wheel passages is too expensive in terms of computational resources. Therefore, two different rail surface geometries are simulated to verify the first two steps during the development process of squats hypothesized in Section 3.

In the first step, the rail surface is assumed to be smooth without any geometric irregularities but with measured spatially varying yield stresses at the weld, as described in Section 4.2. The rolling of a wheel over a rail is simulated with the model and loading described above. It is expected that geometric irregularities will arise, due to the HAZs and the loading, on the rail surface after the wheel passage across the weld. These simulated surface irregularities are compared with field observations and measurements.

In the second step, the surface irregularities derived from the simulation in Step 1 are applied to the rail surface of the FE model to examine the effects of the dynamic force resulted from the irregularities and the trend of the V-shaped dips developing into W-shaped surface patterns at the HAZs. The varying yield stress distribution is assumed to be the same as that of Step 1. In this step, the fastening system is modeled by two groups of springs and dampers to include fastening degradation under wheel-rail interaction [43]. In Step 1, the fastening system is modeled by twelve groups of springs and dampers, ensuring more uniform contact between the rail bottom and the sleeper.

### 5. Simulation of rail profile evolution considering deformation and wear

#### 5.1. Step 1: Formation of V-dips from smooth rail with varying yield stress

##### 5.1.1. Calculated deformation and wear

In this section, the contact stress, plastic deformation and wear simulated at the thermite weld are presented for the smooth rail profile.

Fig. 13 shows the von Mises stress distribution when the wheel-rail contact patch starts to enter the left HAZ. Large stress exceeding the yield stress occurs at the rail surface. This finding suggests that plastic

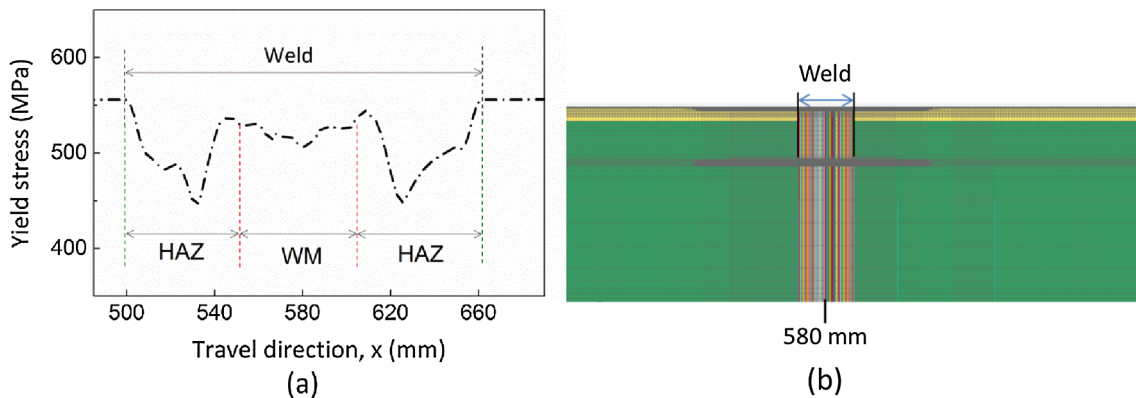


**Fig. 12.** Distribution of yield stress: (a) at the thermite weld derived from Fig. 9(b) and Eq. (1); (b) its implementation in the FE model. (The middle point of the varying yield stress is at the rail location of 580 mm.)

deformation primarily occurs at the rail surface. Therefore, the plastic deformation at the surface should be closely examined.

The calculated vertical plastic deformation  $dz$  and wear exhibit spatially (3D) differential distributions at the weld. Fig. 14 shows the 2D deformation and wear along the center of the running band. It is considerably greater in the HAZs than in the parent rail and the WM. The greatest value is approximately 50% larger than that in the parent rail surface. Plastic deformation also occurs in the WM. The differential deformation generally follows the variation of the initial hardness with the two V-shaped dips in the HAZs.

The varying yield stress also gives rise to differential wear distribution, as shown in Fig. 14. Its pattern, however, does not follow the variation of the hardness. For instance, the greatest wear is in the middle part of the left HAZ rather than at the location of the hardness dip. Therefore, there is a phase shift between the wear and the plastic deformation. A possible reason for this shift is that the micro-slip and surface shear stress that determine the wear are disproportionately affected by the varying hardness distribution, unlike the case for plastic deformation. To fully understand the root cause, further detailed study of the contact behaviors is needed.

#### 5.1.2. Deriving V-dip irregularities from deformation

Rail surface irregularities can be formed by superposition of the accumulated differential plastic deformation and wear. Here, they can be derived from the simulation results of plastic deformation and wear in Fig. 14. In the results, the magnitude of plastic deformation is much larger than that of the wear, and the wear does not follow the hardness distribution. This finding indicates that in the first contact cycles, plastic deformation would dominate the formation of the surface irregularities. With an increase in wheel passages, the plastic deformation per passage will decrease and shakedown will set in due to work hardening. This can be further investigated by simulation of multiple cycles of wheel passages to compare the accumulated plastic deformation and wear. In the present study, it is assumed that the generated irregularities follow the pattern of the plastic deformation. This assumption will be verified in Step 2 by checking whether the typical W-shaped pattern of squats could be formed based on this assumption. Thus there are two V-shaped irregularities due to the plastic deformation in the two HAZs. Additionally, the differential plastic deformation produces a slight central valley in the WM, corresponding to the

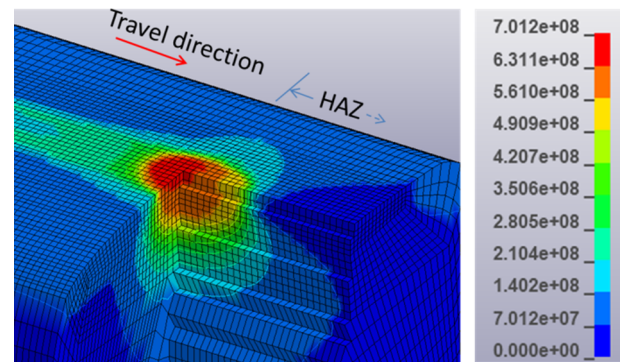


**Fig. 13.** Von Mises stress distribution when the contact patch is entering the left HAZ.

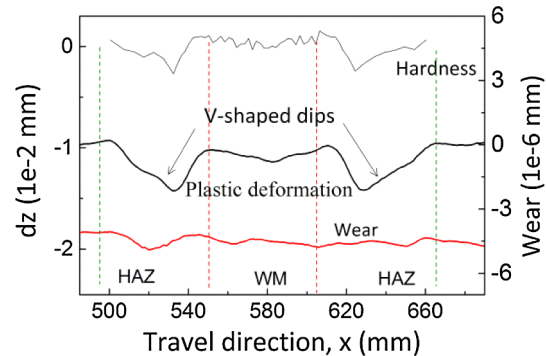


**Fig. 14.** Surface vertical plastic deformation  $dz$  and wear (average smoothing within a radius of 5.5 mm) of Step 1 along the center of the running band at the thermite weld (negative ordinates mean that the directions of deformation and wear are downwards relative to the initial (smooth) rail surface).

hardness distribution in this area.

#### 5.1.3. Comparing the simulation with field measurement

The derived geometric irregularities of the two V-shapes and central valley are in agreement with measured surface irregularities such as

**Table 1**

Material properties of the wheel and the rail.

Components	Elastic modulus (GPa)	Poisson's ratio	Yield stress (MPa)	C (GPa)	$\gamma$	$H$
Surface of wheel & rail	210	0.3	556	41	58	0
Subsurface of wheel & rail	210	0.3	546	41	58	0
Weld	210	0.3	Varied according to Fig. 12	41	58	0

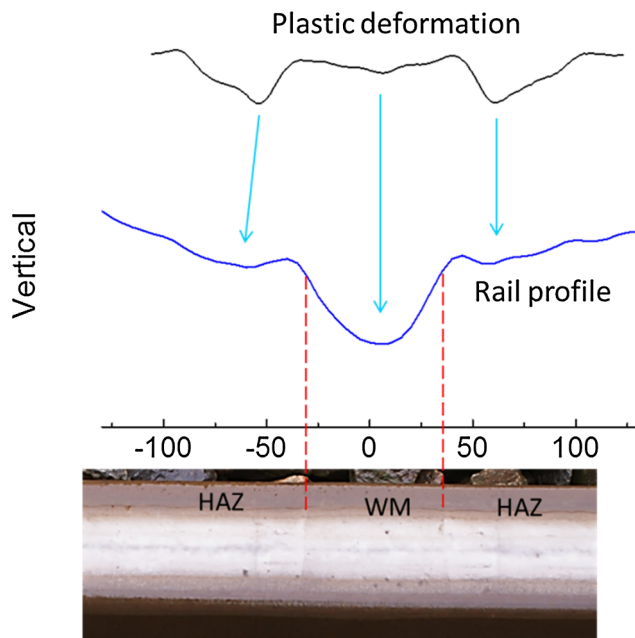


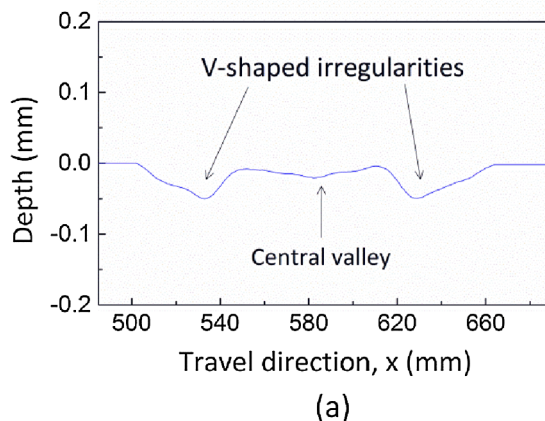
**Fig. 15.** Comparison of the calculated surface irregularities due to plastic deformation (upper curve) in Step 1 with the surface irregularities measured at the thermite weld of Fig. 7(b) (lower curve).

shown in Figs. 7 and 8, especially that of Fig. 7(b), with which a comparison is made in Fig. 15. The occurrence of the two V-shaped irregularities due to the varying material properties in the HAZs and their correspondence to the variation of the hardness distribution confirm Step 1 of the hypothesis of Section 3.

## 5.2. Step 2: Formation of W-shapes from V-dips with varying hardness

### 5.2.1. Generating rail surface with V-dips

At the beginning of Step 2, the surface irregularities due to plastic deformation derived in Step 1 are applied to the rail surface. The derivation is done by setting the largest depth of the left V-dip to 0.05 mm, which is close to the measurement in Fig. 2(b). This means that the deformation is scaled up by a factor of 10.4 to account for multiple wheel passages. The rest of the profile is set proportionally by the same scaling factor. The resulting rail surface is shown in Fig. 16 in 2D and 3D.



(a)

### 5.2.2. Formation of W-shaped patterns and comparison with field measurement

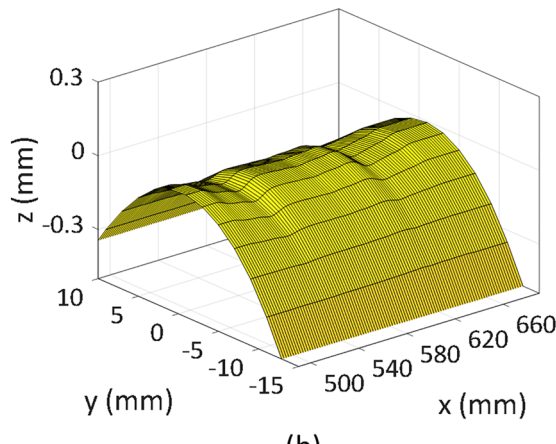
In Fig. 17(a) the plastic deformation (black line) and wear (orange line) calculated from the rail surface of Fig. 16 and average-smoothed within a radius of 5.5 mm are shown together with the start rail profile (dashed blue line) of Step 2, i.e., the profile of Fig. 16(a), along the center of the running band. Again the deformation and wear are differential, and the deformation per cycle is much larger than the wear. By multiplying the deformation by a factor of 10 to account for the effect of multiple wheel passages and adding it to the initial profile (i.e., Fig. 16(a)), an updated rail profile (red line) is obtained in Fig. 17(b). The following observations can be made from this profile:

- (1) The two V-shaped dips of Fig. 16(a) develop into two W-shaped patterns (Fig. 17(b)), with the shortest wavelength being 24 mm between b2-c2 and the longest being 38 mm (a2-b2). The central valley becomes deeper.
- (2) The wavelength of the W-shapes follows that of the longitudinal contact force, see Fig. 17(c), whereas the fluctuation of the vertical force follows the profile that excites it, and the wavelength of the vertical and longitudinal contact forces are different, as indicated by the vertical dashed lines in Fig. 17(c). These are in agreement with the findings of [24], where it was shown that the longitudinal and vertical forces of wheel-rail contact are not necessarily of the same wavelength. The vertical contact force has a strong dependence on the excitation, i.e., rail surface irregularities – rail corrugation, and the longitudinal contact force dominates the initiation of the corrugation. In [15,16,21], it was pointed out that squats are related to short pitch corrugation.
- (3) Correspondence can be found between the simulated W-shaped patterns of Fig. 17(b), indicated by the peaks a2 – f2, and the measured W-shaped patterns with peaks a1 – f1 of Fig. 17(d), though the wavelengths differ, with the wavelengths in the simulation being more uniform (the shortest is 24 mm and longest 38 mm). Among the measured wavelengths, the shortest is 15 mm between e1 – f1, and the longest is 47 mm between a1 – b1. This difference in wavelength will be discussed in Section 6.1. Note that the WM does not belong to the W-shapes.

## 6. Discussions

### 6.1. W-shape is determined by the wavelength of the local dynamic system

The difference in the wavelengths between a1-f1 and a2-f2 can be explained by considering the irregularities a1-f1 as being in a stage



(b)

**Fig. 16.** Rail surface at the beginning of Step 2, obtained from the plastic deformation calculated in Step 1: longitudinal rail profile with two V-shaped irregularities at HAZs and one slight central valley at the WM. (a) Vertical-longitudinal profile and (b) the rail surface in 3D.

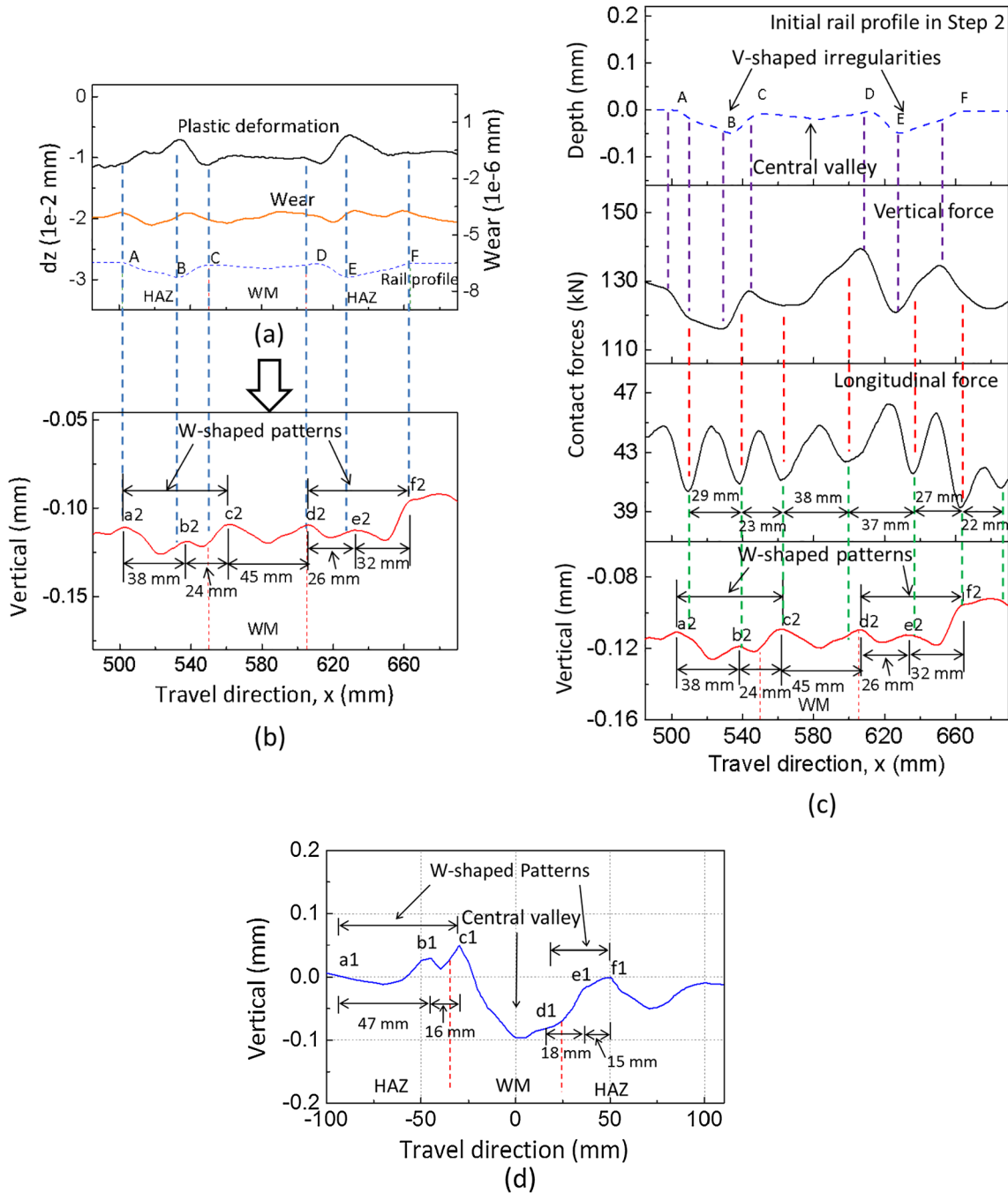


**Fig. 17.** Development of the profile along the center of the running band in Step 2 and comparison with a field measurement: (a) calculated plastic deformation and wear vs. rail profile at the beginning of Step 2; (b) the resulted profile (6 points average smooth) by adding 10 times of the plastic deformation to the initial profile of Step 2; (c) vertical and longitudinal contact forces vs. the excitation (initial rail profile in Step 2) and the resulted profile (the lowest profile is the same as that in Fig. 17(b)); (d) measured profile at a weld (the same as Fig. 2(b)).

different from that of a2-f2 in the development.

The irregularities started as V-shaped dips between ABC and DEF arising from a smooth rail surface, following the hardness variation in the HAZs (Fig. 17(a)). The V-dips excite a dynamic longitudinal contact force of a certain wavelength determined by the local wheel-track system [24], causing differential deformation of the same wavelength. This deformation adds to the irregularities, causing them to evolve from V-dips to W-shapes, with new peaks arising in the initially large V-dips, as discussed for Figs. 2, 7 and 8 in Section 2.2, highlighted with the red arrows in Fig. 7(b) and 8. In Fig. 17 the new peaks are b2 and e2. The new peaks divide an initially large V-dip into two smaller V's to form a W-shape.

The new W-shapes are in phase with the differential plastic deformation in Fig. 17(a), indicating that the resulting geometric irregularities follow the differential plastic deformation. This fact also confirms the assumption in Step 1, wherein V-shaped irregularities follow the pattern of plastic deformation, as discussed in Section 5.1.2.

The differential deformation due to the longitudinal force is not necessarily in phase with the deformation caused by the hardness variation. Thus, the new peaks do not necessarily divide an initially large V into two equal small V's. This makes the wavelength of the initial W-shape non-uniform, as seen in Fig. 17(b), where it varies between 24 and 38 mm, and in Fig. 17(d), where it varied between 15 and 47 mm. This non-uniform wavelength could be considered the result of

the variation in the uniform wavelength of the longitudinal contact force disturbed by the V-dips of the hardness variation. For instance, the wavelength of the longitudinal force, frequently embodied in the wavelength of the short pitch corrugation, is usually around 30 mm in the Dutch railway network [24]. This wavelength is disturbed when there are rail surface irregularities, as shown in Fig. 17. Another example of disturbed wavelength is in Fig. 8, where it is between 27 and 35 mm.

Once a W-shape exists, it also excites the local wheel-track dynamic system, causing deformation and wear of the same wavelength and phase as those of the W-shape. This process forms a loop of positive feedback that leads to the dominance of the W-shape over the V-shape. The uniform wavelength of the longitudinal contact force and the dominance of the W-shape would then gradually change the initially non-uniform wavelength to be more or less uniform.

This change of wavelength could be seen in Fig. 2: a shining R-strip corresponding to the position b1 existed in the 09-2007 photo. It could have occurred due to a hardness jump next to the fusion line, as indicated by the P arrow in Fig. 9, that caused differential deformation. The shining brightness of the R-strip and the depressions on the two sides of it indicate impact-like wheel-rail contact [15]. This dynamic interaction obviously widened the depression between b1c1 in both directions into the wider b1'c1' in 11-2009. Thus, the wavelength of b1c1 was extended. Gradually the width of the two dark depressions, i.e., the wavelength of the two V's in a W-shape, of a squat becomes approximately equal, as seen in the mature squats of Figs. 1–6.

In the development process of the two initial V-dips in the two HAZs of a weld, they have a similar process but possibly different growth rates and different morphologies. In the beginning, the two V-dips are roughly symmetrical about the WM. Then they simultaneously develop into W-shapes with two V-dips. The initial W-shapes are non-uniform because of the disturbed wavelength of dynamic forces by the initial V-dips. Therefore, the morphology of the initial W-shapes could be different. One may have a larger dimension at the front V-dip, while another one may have a larger dimension at the rear V-dip. Moreover, the two W-shapes could grow at different rates because of variations in the magnitudes of dynamic longitudinal contact forces. These forces depend on the size of the initial V-dips and local vehicle-track system. As a result, one W-shape could be larger than the other in dimension, e.g., the left squat in Fig. 2 looks larger than the right one. Eventually, however, all V-dips tend to become similar over time, and the two squats should become similar in both dimension and morphology.

## 6.2. The presence of single or duo squats is determined by length of welds

A flash butt weld usually has a shorter characteristic length of initial hardness variation. As a result, the two dips of the resulting surface irregularities are much closer than are those at thermite welds. This result can be confirmed by the differential plastic deformation in Fig. 18

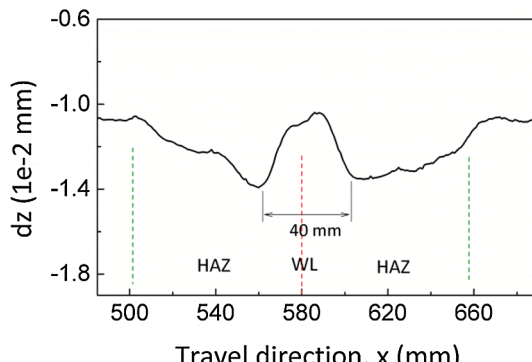


**Fig. 18.** Plastic deformation (average smoothing within a radius of 5.5 mm) along the center of the running band for a flash butt weld with the hardness distribution of Fig. 9(c).

calculated from the hardness distribution of Fig. 9(c). The distance between the two dips is approximately 40 mm, which is within the wavelength of 20–40 mm of typical squats. Thus the two dips combine to form one single W-shaped pattern and, eventually, a single squat.

Similarly, if the characteristic length of the hardness variation in a thermite weld is short, a single squat is likely to occur, such as the squat shown in Fig. 4.

## 6.3. Occurrence or not of squats is determined by both hardness and dynamic contact forces

Occurrence or not of squats at a weld is determined by both welding quality and the eigen characteristics of the local vehicle-track system. If a weld is in good condition where there is no hardness variation or the magnitude of hardness variation is very small in the HAZs, then V-shaped irregularities and subsequent squats are unlikely to take place. This could be the case in the right HAZ of the weld in Fig. 5, where no squat was observed. Even if V-shaped dips are formed due to hardness variation, they can develop into squats only if there exist dynamic forces with a certain wavelength determined by the local wheel-track system. In practice, the quality of welding varies from one weld to another due to inherent limitations of the welding processes and their dependency on human operators [22]. Moreover, the characteristics of the local vehicle-track system are determined by the quality of both tracks and vehicles. Therefore, only the welds that fulfill both conditions at the same time can develop into squats. As both conditions are stochastic and independent from each other, their combination limits the percentage of welds that can develop into squats. However, even a small percentage of welds potentially develop into squats, they significantly affect the safety of railway systems.

## 6.4. Summary

Field observations and measurements, as well as numerical simulations, show that weld-induced squats started from V-shaped dip plastic deformations that followed the initial hardness distribution at the HAZs. The deformations caused a dynamic longitudinal contact force and the resulting differential plastic deformation. The latter added onto the V-shaped dips to cause the initiation and growth of W-shaped irregularities that eventually developed into a typical two-lung-like squat. Each of the lungs was a depression, corresponding to one of the two V's of the W-shape.

Since the hardness-variation induced rail surface irregularities and the resulting dynamic contact forces are the precursors to the squats, it is possible to use a dynamics-based method to detect the squats at an early stage, or even before any fatigue cracks occur. The characteristic wavelength can be used as a signature for detection and monitoring [27,44].

## 7. Conclusions

Five-year continual field monitoring observations and measurements have been performed to investigate the initiation and development of squats at rail welds. Based on these, a three-step hypothesis of the development process of squats at welds is proposed. Steps 1 and 2 are the pre-cracking process, and Step 3 is the post-cracking process. The first two steps are the focus of the present work. Numerical simulations using a 3D FE dynamic vehicle-track interaction model have been performed by considering the varying yield stress based on measured hardness and surface irregularities. The numerical results are in agreement with the field observations, verifying the first two steps of the hypothesis. The conclusions are as follows.

- (1) Squats at welds developed from surface irregularities without cracks.
- (2) In Step 1, initial surface V-shaped irregularities are predominately

- caused by differential plastic deformation that follows the initial varying hardness distribution in the HAZs. Imperfect finish grinding is not necessarily the cause of squats, although it could produce geometric deviation, promoting the development of squats.
- (3) In Step 2, the V-shaped irregularities cause a dynamic longitudinal contact force and the resulting differential plastic deformation. The latter adds onto the V-shaped irregularities to cause the initiation and growth of W-shaped irregularities that eventually develop into typical two-lung-like squats. Each of the lungs is a depression, corresponding to one of the two V's of the W-shape.
- (4) In the development process, the role of the varying hardness distribution is to cause the initial V-shaped rail surface irregularities. The irregularities subsequently cause dynamic longitudinal contact force which determines the W-shape and the eventual typical two-lung shape of mature squats. Here, the dominant characteristic is the wavelength of the longitudinal contact force, which is determined by the local wheel-track system. From the numerical simulation and field observation, this characteristic wavelength of the contact force for the squats appears to be the same as that of the short pitch corrugation.
- (5) The development of the W-shaped irregularities continuously increases the dynamic contact force at the same location, resulting in a positive-feedback growth loop of the irregularities and the dynamic force, leading to rail fatigue and cracks.
- (6) The numerical simulations showed that the irregularity magnitude caused by plastic deformation in a wheel passage is much larger than that caused by wear. This finding needs further investigation to verify. Besides, hardening will occur under repeated wheel-rail rolling contact. As a consequence, hardness and yield stress will evolve over time. The effects of this evolution on the development of surface irregularities is another topic for further research. Further research should also investigate whether white etching layers occur on rail surface around welds and how they influence the hardness variation since they are sometimes observed on rail surfaces, e.g., [45]. Moreover, the material of WM is considered the same type as the parent rail steel. Further work is needed to investigate the effects of more material parameters, such as elastic modulus, plastic hardening modulus and  $n$  in Eq. (1).
- (7) The number of squats induced by a weld is determined by the characteristic length of the initial hardness variation or the quality of welding. Duo squats are frequently observed at thermite welds because the characteristic length is usually much larger than the typical wavelength of squats, i.e., 20–40 mm. A single squat usually occurs at flash butt welds because the characteristic length is in close agreement with that of typical squats. Single squats occur at some thermite welds due to short characteristic length or good quality of welding, indicating that by improving welding quality, weld-induced squats can be reduced or even avoided.
- (8) Since the hardness variation-induced rail surface irregularities and the resulting dynamic contact force are the precursors to the squats, it is possible to use a dynamics-based method to detect squats at an early stage or even before any fatigue cracks occur. The characteristic wavelength can be used as a signature for detection and monitoring.

## References

- [1] Myers J, Geiger G, Poirier D. Structure and properties of thermite welds in rails. *Welding J* 1982;61:258–68.
- [2] Micanco P, Li H. Double dip hardness profiles in rail weld heat-affected zone: literature and research review report, Brisbane, Australia; 2013.
- [3] Steenbergen MJMM, Esveld C. Relation between the geometry of rail welds and the dynamic wheel - rail response: Numerical simulations for measured welds. *Proc Instit Mech Eng, Part F: J Rail Rapid Transit* 2006;220:409–23.
- [4] Ilić N, Jovanović MT, Todorović M, Trtanj M, Šaponjić P. Microstructural and mechanical characterization of postweld heat-treated thermite weld in rails. *Mater Charact* 1999;43:243–50.
- [5] Skyttebol A, Josefson BL, Ringsberg JW. Fatigue crack growth in a welded rail under the influence of residual stresses. *Eng Fract Mech* 2005;72:271–85.
- [6] Fry GT, Lawrence FV, Robinson AR. A model for fatigue defect nucleation in thermite rail welds. *Fatigue Fract Eng Mater Struct* 1996;19:655–68.
- [7] Desimone H, Beretta S. Mechanisms of mixed mode fatigue crack propagation at rail butt-welds. *Int J Fatigue* 2006;28:635–42.
- [8] Wen Z, Xiao G, Xiao X, Jin X, Zhu M. Dynamic vehicle-track interaction and plastic deformation of rail at rail welds. *Eng Fail Anal* 2009;16:1221–37.
- [9] Li W, Xiao G, Wen Z, Xiao X, Jin X. Plastic deformation of curved rail at rail weld caused by train-track dynamic interaction. *Wear* 2011;271:311–8.
- [10] Gao J, Zhai W, Guo Y. Wheel-rail dynamic interaction due to rail weld irregularity in high-speed railways. *Proc Instit Mech Eng, Part F: J Rail Rapid Transit* 2018;232:249–61.
- [11] Sichani MSh, Bezin Y. Differential wear modelling – Effect of weld-induced material inhomogeneity on rail surface quality. *Wear* 2018;406–407:43–52.
- [12] Al-Juboori A, Wexler D, Li H, Zhu H, Lu C, McCusker A, et al. Squat formation and the occurrence of two distinct classes of white etching layer on the surface of rail steel. *Int J Fatigue* 2017;104:52–60.
- [13] Cannon D, Edel KO, Grassie S, Sawley K. Rail defects: an overview. *Fatigue Fract Eng Mater Struct* 2003;26:865–86.
- [14] Clayton P, Allery M. Metallurgical aspects of surface damage problems in rails. *Can Metall Quart* 1982;21:31–46.
- [15] Li Z, Zhao X, Esveld C, Dollevoet R, Molodova M. An investigation into the causes of squats—Correlation analysis and numerical modeling. *Wear* 2008;265:1349–55.
- [16] Li Z, Dollevoet R, Molodova M, Zhao X. Squat growth—Some observations and the validation of numerical predictions. *Wear* 2011;271:148–57.
- [17] Li Z. Squats on railway rails. *Wheel-Rail Interface Handbook*. Woodhead Publishing; 2009. p. 409–36.
- [18] Wei Z, Núñez A, Li Z, Dollevoet R. Evaluating degradation at railway crossings using axle box acceleration measurements. *Sensors* 2017;17:2236.
- [19] Li Z, Zhao X, Dollevoet R. An approach to determine a critical size for rolling contact fatigue initiating from rail surface defects. *Int J Rail Transport* 2017;5:16–37.
- [20] Li Z, Zhao X, Dollevoet R, Molodova M. Differential wear and plastic deformation as causes of squat at track local stiffness change combined with other track short defects. *Veh Syst Dyn* 2008;46:237–46.
- [21] Deng X, Qian Z, Li Z, Dollevoet R. Investigation of the formation of corrugation-induced rail squats based on extensive field monitoring. *Int J Fatigue* 2018;112:94–105.
- [22] Mutton P, Alvarez E. Failure modes in aluminothermic rail welds under high axle load conditions. *Eng Fail Anal* 2004;11:151–66.
- [23] EN 14587-2. Railway applications—track-flash butt welding of rails—Part 2: New R220, R260, R260Mn and R350HT Grade Rails by Mobile Welding Machines at Sites Other Than a Fixed Plant, European Committee for Standardization, Brussels; 2009.
- [24] Li S, Li Z, Nunez Vicencio A, Dollevoet R. New insights into the short pitch corrugation development enigma based on 3D-FE dynamic vehicle-track coupled modelling in frictional rolling contact. *Appl Sci (Switzerland)* 2017;7.
- [25] Saita K, Karimine K, Ueda M, Iwano K, Hiroguchi TYK. Trends in rail welding technologies and our future approach. *Nippon Steel Sumitomo Metal Technical Report* 2013:84.
- [26] Zhao X, Li Z, Liu J. Wheel-rail impact and the dynamic forces at discrete supports of rails in the presence of singular rail surface defects. *Proc Instit Mech Eng, Part F: J Rail Rapid Transit* 2011;226:124–39.
- [27] Molodova M, Li Z, Núñez A, Dollevoet R. Validation of a finite element model for axle box acceleration at squats in the high frequency range. *Comput Struct* 2014;141:84–93.
- [28] Benson DJ, Hallquist JO. A single surface contact algorithm for the post-buckling analysis of shell structures. *Comput Methods Appl Mech Eng* 1990;78:141–63.
- [29] Hallquist J, Goudreau G, Benson D. Sliding interfaces with contact-impact in large-scale Lagrangian computations. *Comput Methods Appl Mech Eng* 1985;51:107–37.
- [30] Zhao X, Li Z. The solution of frictional wheel–rail rolling contact with a 3D transient finite element model: Validation and error analysis. *Wear* 2011;271:444–52.
- [31] Zhao X, Li Z. A three-dimensional finite element solution of frictional wheel–rail rolling contact in elasto-plasticity. *Proc Instit Mech Eng, Part J: J Eng Tribol* 2015;229:86–100.
- [32] Deng X, Qian Z, Dollevoet R. Lagrangian explicit finite element modeling for spin-rolling contact. *J Tribol* 2015;137:041401–11.
- [33] Cahoon J, Broughton W, Kutzak A. The determination of yield strength from hardness measurements. *Metall Mater Trans B* 1971;2:1979–83.
- [34] Tapp C. Mechanische Eigenschaften von Schienenstählen nach zyklischer Verformung. VDI-Verlag; 2005.
- [35] Esveld C. Modern Railway Track. The Netherlands: MRT-Productions; 2001.
- [36] Lemaître J, Chaboche J-L. Mechanics of solid materials. Cambridge University Press; 1994.
- [37] Kabo E, Ekberg A, Torstensson PT, Vernersson T. Rolling contact fatigue prediction for rails and comparisons with test rig results. *Proc Instit Mech Eng, Part F: J Rail Rapid Transit* 2010;224:303–17.
- [38] Johansson G, Ahlström J, Ekh M. Parameter identification and modeling of large ratcheting strains in carbon steel. *Comput Struct* 2006;84:1002–11.
- [39] Olofsson U, Nilsson R. Surface cracks and wear of rail: A full-scale test on a commuter train track. *Proc Instit Mech Eng, Part F: J Rail Rapid Transit* 2002;216:249–64.
- [40] Archard J. Contact and rubbing of flat surfaces. *J Appl Phys* 1953;24:981–8.
- [41] Perez J, Sinclair J, Tunna J. A review of wheel wear and rolling contact fatigue. *Proc Instit Mech Eng, Part F: J Rail Rapid Transit* 2007;221:271–89.
- [42] Olofsson U, Telliskivi T. Wear, plastic deformation and friction of two rail steels—a full-scale test and a laboratory study. *Wear* 2003;254:80–93.
- [43] Zhao X, Li ZL, Dollevoet R. Influence of the fastening modeling on the vehicle-track interaction at singular rail surface defects. *J Comput Nonlinear Dyn* 2014;9.
- [44] Molodova M, Li ZL, Nunez A, Dollevoet R. Automatic detection of squats in railway infrastructure. *IEEE Trans Intell Transp* 2014;15:1980–90.
- [45] Kumar A, Agarwal G, Petrov R, Goto S, Sietsma J, Herbig M. Microstructural evolution of white and brown etching layers in pearlitic rail steels. *Acta Mater* 2019;171:48–64.